communications earth & environment

Article

https://doi.org/10.1038/s43247-024-01400-z

Hydrothermal sulfidation of biogenic magnetite produces framboid-like pyrite

Check for updates

Eric Runge [1,2] ✉, Muammar Mansor [3], Tsz Ho Chiu [3], Jeremiah Shuster[4,5], Stefan Fischer[4], Andreas Kappler [3,6] & Jan-Peter Duda [1,2] ✉

Biogenic magnetite is a potential biosignature for microbial iron cycling in hydrothermal sulfide systems, critical environments for unraveling the emergence and early evolution of life. However, the preservation potential of biogenic magnetite under hydrothermal conditions is poorly understood. Here, we show that the hydrothermal sulfidation of abiogenic and biogenic magnetite (sulfide/iron = 4, 80 °C) yields pyrite with various distinct morphologies, including framboid-like spheroids. We demonstrate that the variability in pyrite morphologies resulted from the modulation of pyritization rates by interrelated effects between organic matter and elemental sulfur (crystalline or colloidal). Notably, framboid-like pyrite, commonly considered a potential fingerprint of microbial sulfur cycling, was exclusively produced from the hydrothermal sulfidation of biogenic (i.e., organic matter-associated) magnetite produced by iron-cycling microorganisms. Thus, framboid-like pyrite can additionally be a taphonomic fingerprint of microbial iron cycling, enabling a better understanding of the evolution of Earth's biosphere in deep time.

Hydrothermal systems are prime environmental candidates for life's emergence due to their potential role in prebiotic organic synthesis[1–3], their steep physical and chemical gradients establishing disequilibrium conditions[4,5], and their existence on Earth for at least 3.77 billion years[2,6–10]. Hydrothermal systems potentially occurred in past surface environments on early Mars[11] and in modern subsurface oceans of Enceladus[12], underscoring their astrobiological significance. Therefore, understanding the proliferation of a microbial biosphere under hydrothermal conditions is crucial. This task requires tools for unraveling the interactions of minerals, organic compounds, and microorganisms in hydrothermal systems on the early Earth. Microbial biosignatures in early Earth's rock record are our only archive for investigating these interactions in deep time[10]. Thus, better constraining the formation and preservation of microbial biosignatures in ancient hydrothermal deposits is fundamental for understanding the emergence and subsequent evolution of life on our planet and beyond.

Nano-magnetite [Fe_3O_4] is an essential piece in this puzzle due to its ubiquitous bio-mediated formation in early Earth's oceans and its potential role in catalyzing vital prebiotic chemical reactions in hydrothermal systems[1,13,14]. On modern Earth, nano-magnetite forms by abiotic Fe(II)-driven transformation of Fe(III) (oxyhydr)oxides or via iron-cycling microorganisms, such as dissimilatory Fe(III)-reducing prokaryotes or magnetotactic bacteria[15–17]. Dissimilatory Fe(III)-reducing prokaryotes and magnetotactic bacteria are thought to have emerged in the Archean[18,19], and commonly occur in modern hydrothermal sulfide environments[20–23]. Indeed, strain 121 (*Geogemma barossii*), one of the most heat-tolerant microorganisms known on Earth to date, is a magnetite-producing Fe(III)-reducing archaeon isolated from a black smoker system[24], highlighting the role of magnetite biomineralization under hydrothermal conditions. Biogenic magnetite has specific morphologic, crystallographic, magnetic, and geochemical properties that differ from abiogenic magnetite[15,25–31]. Biogenic magnetite is also closely associated with organic matter, namely the cells and extracellular polymeric substances of microorganisms involved in its formation[28,30]. These properties make biogenic magnetite a potential biosignature of iron-cycling microorganisms in hydrothermal environments.

In hydrothermal environments, magnetite might be affected by sulfide delivered from hot and acidic fluids (up to ~400 °C; pH 2–5)[32] and microbial sulfur cycling[33], likely exerting a dominant control on its preservation[34]. This is because sulfide can drive the rapid reductive dissolution of nano-magnetite[34–40]. Magnetite sulfidation leads to the formation of secondary iron sulfides, including mackinawite [FeS_m], greigite [Fe_3S_4], and pyrite

[1]Sedimentology and Organic Geochemistry, Department of Geosciences, Tübingen University, Tübingen, Germany. [2]Department of Geobiology, Geoscience Center, University of Göttingen, Göttingen, Germany. [3]Geomicrobiology, Department of Geosciences, Tübingen University, Tübingen, Germany. [4]Tübingen Structural Microscopy Core Facility, Tübingen University, Tübingen, Germany. [5]Department of Earth Sciences, Western University, London, ON, Canada. [6]Cluster of Excellence EXC 2124, Controlling Microbes to Fight Infection, Tübingen University, Tübingen, Germany. ✉e-mail: eric.runge1@uni-goettingen.de; jan-peter.duda@uni-goettingen.de

[FeS_2][34,35,39]. The mechanisms and rates of these reactions, and the potential transformation of secondary iron sulfides to pyrite, are affected by temperature, solution E_h and pH, sulfur/iron ratio, magnetite stoichiometry, and the presence of trace metal(loid)s[34,39–48]. Moreover, elemental sulfur [S^0], a ubiquitous intermediate sulfur species in hydrothermal systems, can strongly affect magnetite pyritization rates and pyrite morphology[34]. This implies that diagenetic processes in hydrothermal sulfide systems substantially alter biosignatures associated with magnetite.

Previous studies have not considered the interrelated effects of sulfur species (i.e., sulfide, S^0, polysulfides) with organic matter (e.g., microbial biomass) that would be present during the hydrothermal sulfidation of biogenic magnetite. Organic matter is known to affect the surface reactivity and aggregation behavior of Fe(III) (oxyhydr)oxides, including magnetite, and secondary iron (mono)sulfides[47,49–53]. This potentially influences the textural and geochemical characteristics of the resulting pyrite, which commonly serves as a biosignature of sulfur-cycling microorganisms. For instance, pyrite exhibiting a framboidal morphology is widely used to track microbial sulfur cycling, especially if it encodes ^{34}S-depleted sulfur stable isotope signatures ($\delta^{34}S_{source}$ - $\delta^{34}S_{pyrite}$ > 20‰)[54–57]. Framboidal pyrite from modern and ancient environments is commonly associated with organic matter, suggesting an essential role of organic templates in its formation[55,56]. However, experimental work on pyrite formation in active sulfur- and iron-cycling microbial cultures, as well as abiotic diagenesis of biogenic FeS (i.e., in the presence of microbial biomass but no living cells) at high temperatures (75–150 °C), yielded <1–5 µm-sized pyrite spheroids that do not show the typical raspberry-like texture commonly seen in framboids[58–61]. Furthermore, some experimental studies without organic matter demonstrated abiotic formation pathways for framboidal pyrite (see review by ref. 62). Nevertheless, while the direct role of microorganisms influencing framboid formation is elusive, organic matter appears to have a strong impact on pyrite morphology in natural environments. However, the identity and morphology of iron sulfides from the sulfidation of biogenic magnetite under hydrothermal conditions have not been constrained.

Here, we demonstrate experimentally that abiogenic and biogenic magnetite sulfidation under sulfidic hydrothermal conditions (60 mM sulfide, 15 mM iron, in anoxic artificial seawater at 80 °C, pH 7.5) yields various pyrite morphologies, including framboid-like spheroids. With µ-X-ray diffraction (µ-XRD), Raman spectroscopy, geochemical analysis ($Fe(II)_{aq}$ and sequential iron extraction), ultraviolet-visible (UV-Vis) spectroscopy, and scanning electron microscopy (SEM) supported by focused-ion-beam (FIB) milling, we show that the interrelated effects of organic matter and S^0 (62 mM) on magnetite sulfidation rates and mechanisms control the variability of pyrite morphotypes. Notably, our study demonstrates that framboid-like pyrite results from the hydrothermal sulfidation of biogenic magnetite but not abiogenic magnetite. Thus, framboid-like pyrite may not only fingerprint microbial sulfur cycling but also record microbial iron cycling in hydrothermal sulfide systems.

Results

Mineralogical analyses

After 7 days of incubation, magnetite was neither detected by µ-XRD nor by Raman spectroscopy in any experimental setup (Figs. 1 and 2). Instead, pyrite formed in all experiments as indicated by characteristic Raman bands at 330–333 cm^{-1} and 366–371 cm^{-1} (Fig. 2). Pyrite is absent from µ-XRD patterns in experiments with abiogenic magnetite crystalline S^0 (Fig. 1). Also, pyrite was not detected by µ-XRD in any experiment with biogenic magnetite (Fig. 1). This could be due to a pyrite content below the limit of detection or a poor degree of crystallinity. Mineral products from experiments with abiogenic magnetite also showed Raman bands characteristic of Fe(III)-containing mackinawite (Fe(III)-FeS_m: 310–319 cm^{-1})[63], but only in the absence of S^0 (Fig. 2). In contrast, all experiments with biogenic magnetite contained Fe(III)-FeS_m (Fig. 2).

After 21 days of incubation, the mineralogical composition of experiments with abiogenic magnetite remained unchanged (Figs. 1, and 2). The appearance of µ-XRD reflections characteristic for pyrite in experiments with both abiogenic and biogenic magnetite (+S^0) may reflect an increasing degree of crystallinity (Fig. 1). In experiments with biogenic magnetite and S^0, Fe(III)-FeS_m was no longer detected using Raman spectroscopy (Fig. 2). In contrast, µ-XRD reflections characteristic of FeS_m are still present (Fig. 1). This is most likely due to the limited spot size during in-situ analysis by Raman spectroscopy.

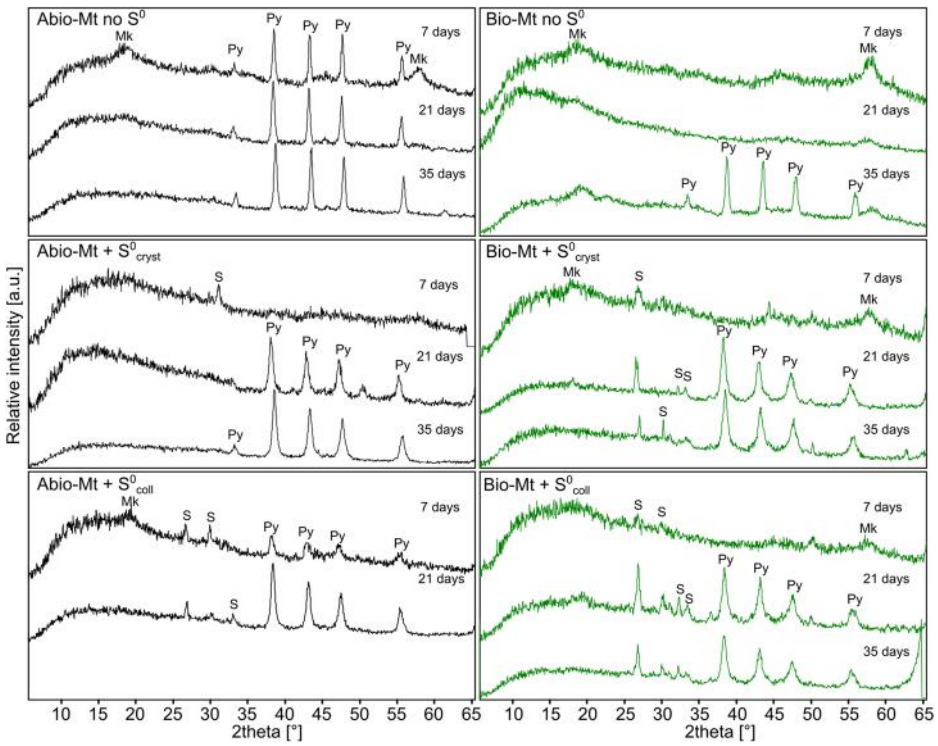

Fig. 1 | µ-XRD patterns for sulfidation experiments with abiogenic magnetite (Abio-Mt, black) and biogenic magnetite (Bio-Mt, green). Mk: Mackinawite; Py: Pyrite; S: S^0. Please note that one sample from the experiment with abiogenic magnetite and colloidal S^0 (35 days) could not be analyzed due to technical problems with the instrument.

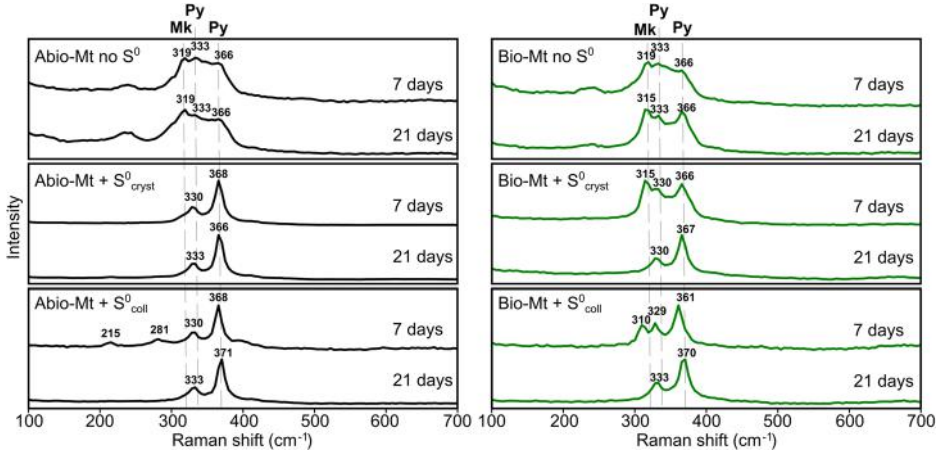

Fig. 2 | Raman spectra for sulfidation experiments with abiogenic magnetite (Abio-Mt, black) and biogenic magnetite (Bio-Mt, green). Mk: Fe(III)-FeS_m, Py: Pyrite. Note that Fe(III)-FeS_m was detected in experiments with biogenic magnetite and S^0 after 7 days but not in experiments with abiogenic magnetite.

After 35 days of incubation, pyrite was detected in experiments with biogenic magnetite (no S^0) using µ-XRD (Fig. 1). Overall, µ-XRD reflections characteristic of pyrite are broader in the presence of S^0 (Fig. 1), indicating greater variability in d-spacing consistent with a lower degree of crystallinity.

Geochemical analysis

In experiments with and without crystalline S^0, $Fe(II)_{aq}$ was between 43–74 µM at t_0 and decreased to <10 µM during the experiment (Fig. 3a, Supplementary Data 1). Much higher $Fe(II)_{aq}$ concentrations occurred in the presence of colloidal S^0 (304 µM and 105 µM with abiogenic and biogenic magnetite, respectively; Fig. 3a). After 3 days of incubation, $Fe(II)_{aq}$ concentrations in experiments with colloidal S^0 were in the range of the other experiments (Fig. 3a).

Sequential iron extraction on the solid phase indicated a much faster increase in the degree of pyritization [$Fe(HNO_3)$/[Fe(HCl) +$Fe(HNO_3)$]] in the presence of S^0 for both abiogenic and biogenic magnetite (Fig. 3b, Table 1, Supplementary Data 1). Pyritization proceeded faster in experiments with colloidal S^0 than with crystalline S^0 for both abiogenic and biogenic magnetite (Fig. 3b, Table 1). Regardless of the presence of S^0, pyritization rates were slower with biogenic magnetite (Fig. 3b, Table 1).

Ultraviolet-visible (UV-Vis) spectroscopy

At the start (t_0), experiments with colloidal S^0 showed increased UV-Vis absorbances across the analyzed spectrum (250–500 nm) compared to all other experiments (Fig. 4a). This is likely due to the presence of colloidal FeS in the supernatant. After 3 days, a yellow coloration of the supernatant indicated the presence of polysulfides in experiments with S^0 (Supplementary Fig. 1[64]), supported by UV absorption peaks at 280 and 314 nm (Fig. 4b[48,65]). Experiments with S^0 showed higher absorbances than experiments without S^0, which indicates a higher abundance of dissolved polysulfides (Fig. 4b–d[65]). In the presence of colloidal S^0, the absorbance of peaks characteristic of polysulfides was higher than in the presence of crystalline S^0 (Fig. 4b–d, Supplementary Fig. 1). Generally, experiments with biogenic magnetite showed higher polysulfide abundances than equivalent experiments with abiogenic magnetite (Fig. 4b–d, Supplementary Fig. 1). Polysulfide abundances and the 314–280 nm absorbance peak ratio in all experiments increased over time (Fig. 4b–e).

Scanning electron microscopy (SEM) and focused-ion-beam (FIB) milling

After 7 days of incubation, all experiments contained platy crystals characteristic of FeS_m (Fig. 5a–f[66,67]). Experiments with abiogenic magnetite but without S^0 further contained µm-sized cubic-euhedral pyrite (Fig. 5a). In the presence of both crystalline and colloidal S^0, experiments with abiogenic magnetite contained octahedral-dendritic pyrite (Fig. 5b, c). No pyrite was

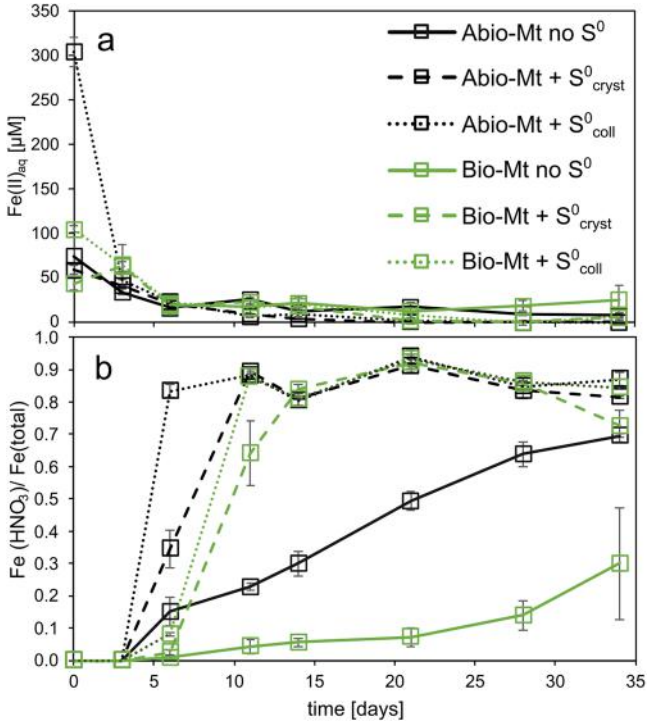

Fig. 3 | Iron geochemistry of sulfidation experiments with abiogenic magnetite (Abio-Mt) and biogenic magnetite (Bio-Mt). The error bars represent the standard deviations of a minimum of experimental duplicates. **a** Aqueous phase ($Fe(II)_{aq}$: combined dissolved and colloidal iron); **b** Degree of pyritization (DOP) as determined via sequential iron extraction of the solid phase using 6 M HCl (magnetite/FeS_m/greigite) and 8 M HNO_3 (pyrite).

observed in experiments with biogenic magnetite, irrespective of the presence of S^0 (Fig. 5d–f). Since Raman spectroscopy and sequential extraction, but not µ-XRD, indicated the presence of pyrite (Figs. 1–3), the precipitates appear to be nano-crystalline.

After 21 days of incubation (Fig. 5g–l), no morphological changes in the precipitates from experiments with abiogenic magnetite were observed (Fig. 5g–i). Also, pyrite remained undetected in experiments with biogenic magnetite but without S^0 (Fig. 5j). However, samples from experiments with biogenic magnetite and crystalline and colloidal S^0 contained ~3–5 µm-sized pyrite spheroids (Fig. 5k, l). FIB sections milled after 47 days of incubation revealed remnant internal grain boundaries within the pyrite spheroids, demonstrating that they consist of aggregates of nm-sized pyrite crystals (Fig. 6).

Table 1 | Degree of pyritization (DOP) after 6 days inferred from sequential iron extraction ($Fe(HNO_3)/Fe(HCl)+Fe(HNO_3)$; see also Fig. 3)

Experiment	DOP (6 days)	SD (1σ)	Apparent pyrite grain size [μm]	Pyrite morphology
Abio-Mt, no S^0	0.15	0.04	2–3	Cubic-euhedral
Abio-Mt, crystalline S^0	0.35	0.06	3–5	Dendritic-octahedral
Abio-Mt, colloidal S^0	0.83	0.02	3–5	Dendritic-octahedral
Bio-Mt, no S^0	0.01	0.00	Nano-crystalline	Nano-crystalline
Bio-Mt, crystalline S^0	0.03	0.01	3–5	Framboid-like spheroid
Bio-Mt, colloidal S^0	0.08	0.00	3–5	Framboid-like spheroid

The faster pyritization rates, indicated by higher DOP, in experiments with abiogenic magnetite and S^0, compared to equivalent experiments with biogenic magnetite or without S^0.

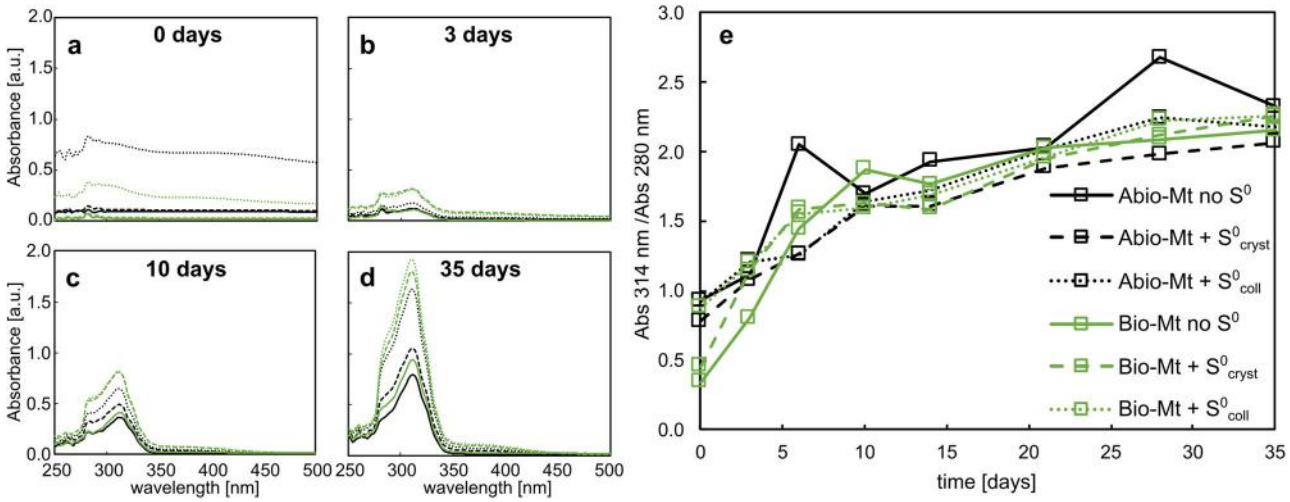

Fig. 4 | UV-Vis spectra of the supernatants in sulfidation experiments with abiogenic magnetite (Abio-Mt) and biogenic magnetite (Bio-Mt). a Increased absorbance in experiments with colloidal S^0, particularly with abiogenic magnetite, likely due to the presence of colloidal FeS (see also Fig. 3a). **b**–**d** Absorption peaks at 280 and 314 nm showing the presence of dissolved polysulfides after 3, 10, and 35 days (**b**, **c**, **d**, respectively). Note that polysulfide abundances are higher in experiments with biogenic magnetite than abiogenic magnetite, with S^0 than no S^0, and with colloidal S^0 than crystalline S^0. **e** Ratios of absorbance peaks at 314 and 280 nm.

Discussion

Magnetite dissolution

The absence of μ-XRD reflections and Raman bands characteristic for magnetite after 7 days (Figs. 1–2) suggests rapid sulfidation of the magnetite precursor in all experiments. This most likely proceeds via the reductive dissolution of magnetite driven by excess aqueous sulfide[34,36], as supported by the initial increase in $Fe(II)_{aq}$ (Fig. 3a). $Fe(II)_{aq}$ likely represents the combined presence of dissolved Fe^{2+}, colloidal FeS particles, and aqueous FeS complexes (Fig. 3a[45,68]). The presence of colloidal FeS in the supernatant is further supported by increased UV-Vis absorbance in these experiments (Fig. 4a). Accordingly, the higher $Fe(II)_{aq}$ concentration in experiments with colloidal S^0 (Fig. 3a) is either due to an increased Fe^{2+} release from magnetite dissolution or a higher abundance of colloidal and/or aqueous FeS. An increased liberation of Fe^{2+} is readily explained by a faster dissolution rate of colloidal S^0 compared to crystalline S^0[69,70], which would release more reactive sulfur species into the system, promoting magnetite dissolution. This is also consistent with higher polysulfide abundances in the presence of colloidal S^0 compared to crystalline S^0 (Fig. 4b–d). Polysulfides generated in this process could also complex Fe^{2+}, leading to a higher abundance of aqueous FeS species[71].

We also observed lower initial $Fe(II)_{aq}$ in experiments with biogenic magnetite relative to equivalent setups with abiogenic magnetite (Fig. 3a). This could be due to the complexation of $Fe(II)_{aq}$ with organic molecules adsorbed to mineral surfaces (Supplementary Fig. 2[50]). Alternatively, organic matter may passivate surfaces or promote the aggregation of magnetite and FeS_m, lowering their dissolution rate and, thus, $Fe(II)_{aq}$ release[47,51,72]. The rapid decrease in $Fe(II)_{aq}$ after 3 days is likely due to the aggregation of colloidal FeS[73]. Subsequently, $Fe(II)_{aq}$ remains low because FeS is poorly soluble at pH 7.5[74].

Polysulfide formation

The higher abundance of polysulfides in the presence of S^0 in our experiments suggests the oxidation of aqueous sulfide by S^0 as a relevant process (Fig. 4b–d). Indeed, this process is known to yield stable polysulfides at pH > 7[70,75], which agrees with our experiment (pH 7.5). In contrast, the possible formation of polysulfides via oxidation of sulfide by Fe(III) in magnetite is most effective at neutral pH[34,45,76] and hence is likely not the dominant mechanism in the case of our experiments. The higher abundance of polysulfides in experiments with colloidal S^0 relative to crystalline S^0 is likely due to the larger reactive surface of colloidal S^0 (Fig. 4b–d[69,70]). Higher abundances of polysulfides in experiments with biogenic magnetite might suggest that organic matter drives the oxidation of aqueous sulfide to secondary S^0[77], which then further reacts with sulfide to polysulfides.

Controls on pyritization rate

FeS_m in our experiments co-exists with pyrite after 7 days and disappears after 21 days (Figs. 1–2, and 5), suggesting that pyritization proceeds via a FeS_m precursor. The faster pyritization rate in experiments with added S^0 (i.e., at a high polysulfide abundance, Figs. 3–4) indicates that pyrite in our experiments dominantly forms via the polysulfide pathway (Eq. (1)),

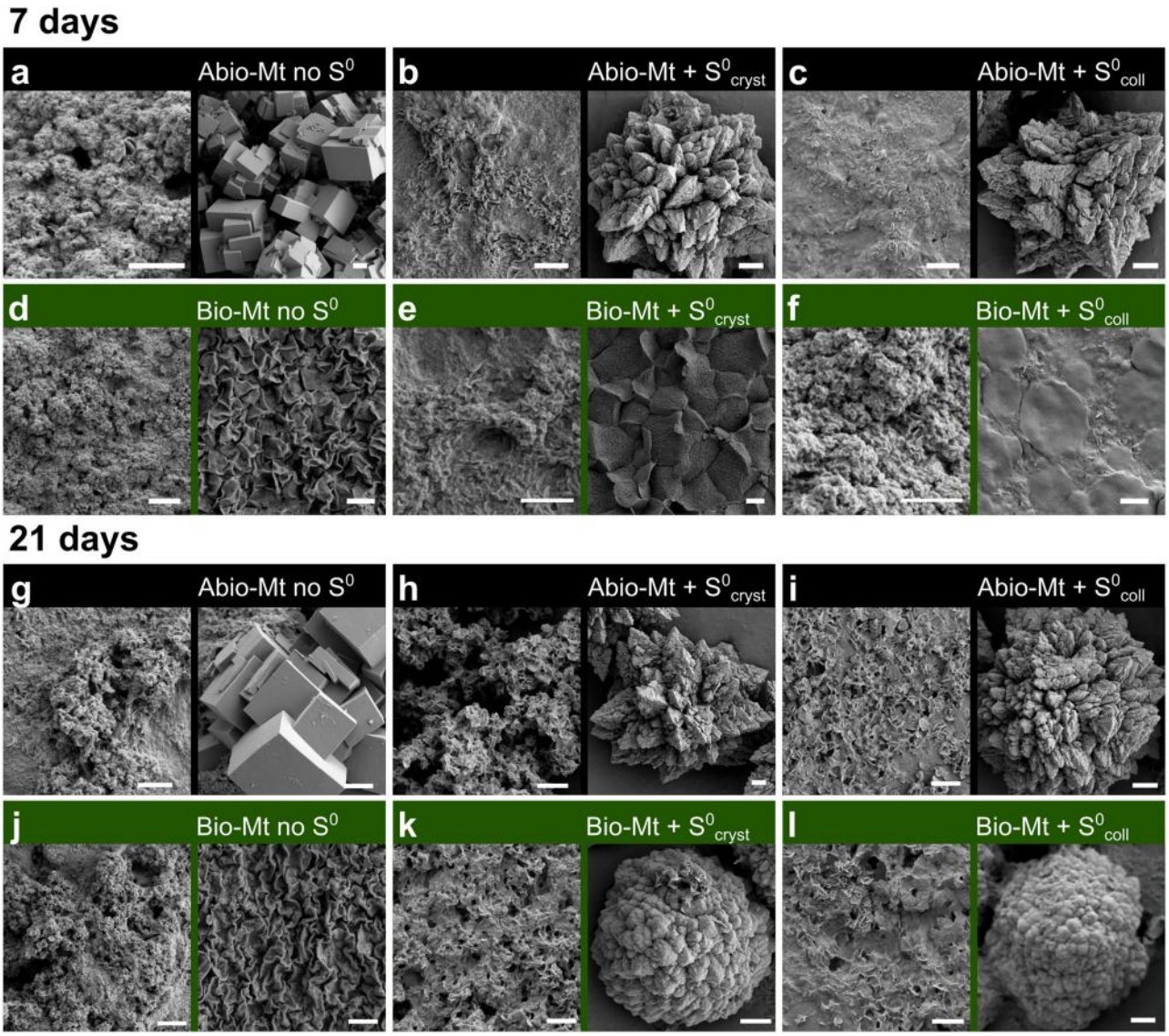

Fig. 5 | SEM images of products from sulfidation of abiogenic magnetite (Abio-Mt, black boxes) and biogenic magnetite (Bio-Mt, green boxes). a–f SEM images after 7 days. **g–l** SEM images after 21 days. FeS_m formed in all experiments. Cubic-euhedral pyrite formed in experiments with neither organic matter (OM) nor S^0 (**a**, **g**). In experiments with biogenic magnetite, no pyrite was observed after 7 days, irrespective of the presence of S^0 (**d**–**f**). Dendritic-octahedral pyrite formed in experiments without OM but with the addition of S^0 (**b**, **c**, **h**, **i**). Framboid-like pyrite spheroids only formed in experiments with OM and S^0 after 21 days (**k**, **l**). All scale bars are 1 μm.

consistent with previous magnetite sulfidation experiments under anoxic conditions[34,39]. Pyrite formation via the polysulfide pathway predicts a change in the polysulfide speciation (i.e., chain length) over time (Eq. (1)[48]). We speculate that the asymptotic increase in the 314–280 nm UV absorption peak ratio during our experiments (Fig. 4e) indicates an overall shift towards shorter polysulfide chain lengths, although individual polysulfide species cannot be discriminated with this technique alone.

$$FeS_{aq} + S_n^{2-} \rightarrow FeS_2 + S_{(n-1)}^{2-} \quad (1)$$

Pyritization rates in experiments with biogenic magnetite were systematically slower than in equivalent setups with abiogenic magnetite, irrespective of the addition of S^0 (Fig. 3). This is consistent with previous studies demonstrating an inhibitory effect of organic compounds on pyrite formation[47,49,51,52] and demonstrates that organic matter has an additional control on reaction rates. Organic matter may protect S^0 or FeS_m against dissolution, potentially resulting in a decreased formation of polysulfides and, consequently, pyrite[78,79]. Moreover, organic matter sulfurization may act as a sink for polysulfides in experiments with biogenic magnetite, which would not be available for pyrite formation[80]. However, biogenic magnetite experiments showed increased abundances of polysulfides at slower pyritization rates (Figs. 3–4); hence, pyritization is not limited by polysulfide abundance. More likely, pyritization is inhibited by the sorption of organic matter to FeS_m, decreasing mineral reactivity towards aqueous (poly)sulfide and limiting its aggregation and/or growth[47,79]. This, in turn, may slow down FeS_m transformation to pyrite, especially at the nm scale[81]. This likely explains the inhibition of pyrite formation in the experiment with biogenic magnetite and no S^0.

Rate control on pyrite morphology

In our experiments with abiogenic magnetite, there is a clear relationship between pyritization rate and morphology (Figs. 5 and 7). Octahedral-dendritic pyrite formed in the presence of S^0 and at faster pyritization rates are morphologically identical to previously reported pyrites from sulfidation of abiogenic magnetite (Figs. 5b, c, h, i and 7[34]). These crystals likely reflect high degrees of supersaturation, resulting in rapid nucleation[34,82,83]. In contrast, cubic-euhedral pyrite is generally associated with lower degrees of

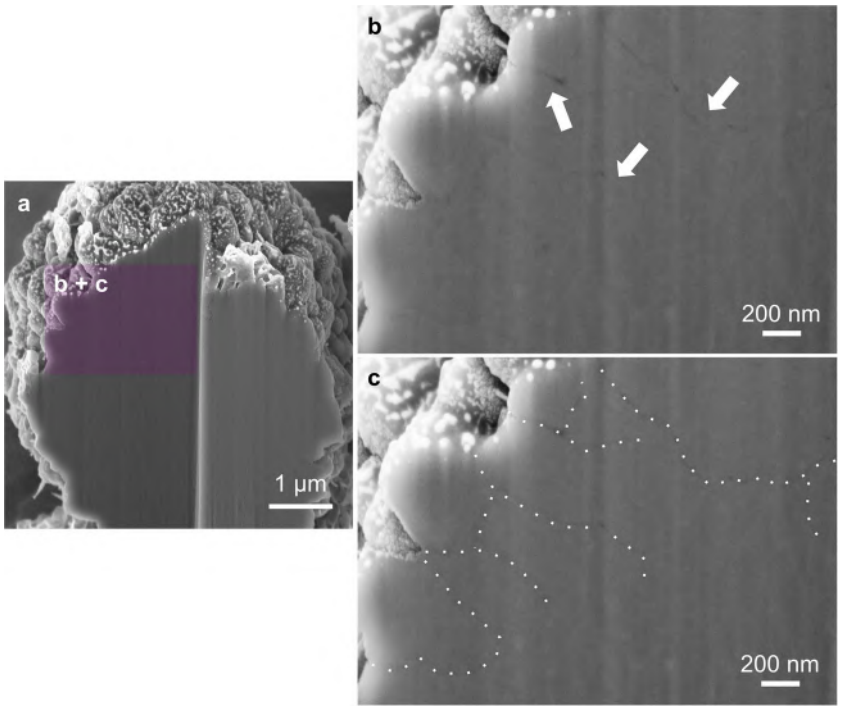

Fig. 6 | SEM images after focused-ion-beam (FIB) milling of a framboid-like pyrite spheroid after 47 days of incubation. a overview of the FIB section. Note the presence of remnant grain boundaries near the edges of the spheroid (white arrows in **b**, white dotted lines in **c**).

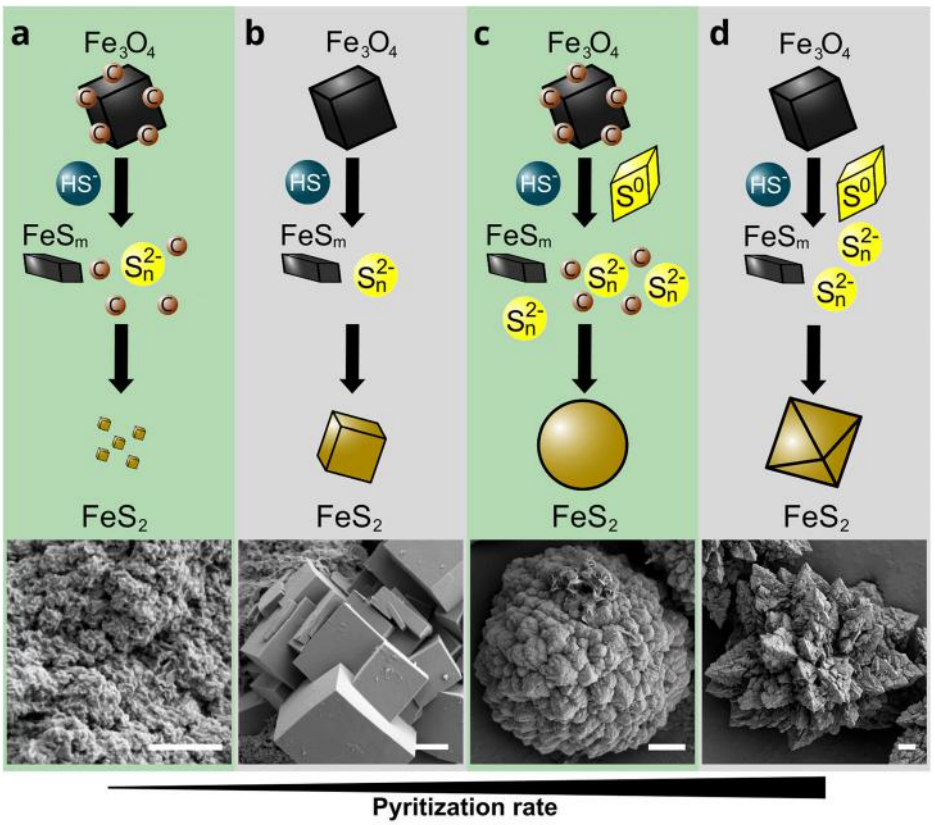

Fig. 7 | Pyrite morphology after sulfidation of abiogenic and biogenic magnetite as a function of pyritization rate and the presence of organic matter (OM). Magnetite is reductively dissolved by aqueous HS^- (and H_2S, not shown), releasing Fe^{2+} (and minor Fe^{3+}, not shown), which reprecipitates as Fe(III)-FeS_m. **a** Sulfidation of magnetite in the presence of OM but without S^0 yields the slowest pyritization rates, resulting in nanoparticulate pyrite (not observed in SEM). **b** Without OM and S^0, pyrite growth is slow, yielding cubic-euhedral pyrite. **c** In the presence of OM and S^0, the pyritization rate is high, and OM mediates the formation of pyrite spheroids. **d** In the absence of OM but in the presence of S^0, pyritization rates are the highest, yielding octahedral-dendritic pyrite. All scale bars are 1 µm.

supersaturation and slower growth rates, allowing for well-developed crystal faces (Fig. 7[82]). This is consistent with µ-XRD data, showing higher degrees of crystallinity than octahedral-dendritic pyrite produced in experiments with abiogenic magnetite and S^0 (Fig. 1).

The slower pyrite growth rates in our experiments with abiogenic magnetite and without S^0 likely resulted from the lower abundance of polysulfides (Fig. 4b–d, Supplementary Fig. 1). Notably, the resulting cubic-euhedral pyrite in this study exhibits a distinctly different habitus than octahedral-dendritic pyrite that formed in previous magnetite sulfidation experiments at equivalent conditions (sulfide/Fe = 4, 62 mM S^0) but slightly lower pH (~7[34] vs. 7.5 in the present study). This effect may be due to pH-dependent polysulfide formation in magnetite suspensions. In our

experiments at pH 7.5, the surface-mediated polysulfide formation was muted[76], possibly yielding an overall lower abundance of polysulfides than at pH 7. This may have inhibited the dominant polysulfide pathway for pyrite formation in our experiments at pH 7.5 without S^0, yielding slower pyritization rates. Hence, this highlights that variations of only 0.5 pH units can substantially affect pyrite morphology.

Influence of organic matter on pyrite morphology

Biological organic matter, such as cell walls, microbial extracellular polymeric substances, or intracellular materials, can provide nucleation sites and templates for pyrite formation[55,56,59]. Furthermore, organic compounds may promote pyrite spheroid nucleation in anoxic experimental systems by increasing E_h[59], substantially influencing pyrite morphology[84]. Organic matter also appears to strongly control pyrite morphology in our experiments. For instance, the slowest pyritization rates were observed in experiments with biogenic magnetite but without S^0 (Fig. 3). Here, pyrite was evidenced with Raman spectroscopy, μ-XRD, and sequential extraction but is not visible in SEM even after 21 days, supporting slow growth to only very small particle sizes (Figs. 5 and 7). Organic matter was suggested to inhibit the growth and transformation of ferrihydrite in the presence of Fe(II) or sulfide via particle aggregation and Ostwald ripening[47,53,85]. Possibly, a similar mechanism affects nanoparticulate pyrite or its precursors, such as FeS_m, in our experiment. On the other hand, experiments with biogenic magnetite and S^0 contained ~3–5 μm-sized pyrite spheroids after 21 days, while no such spheroids were observed after the sulfidation of abiogenic magnetite (Figs. 5 and 7). Based on our data, it cannot be resolved whether templating effects or organic matter-induced kinetic effects primarily drive pyrite spheroid formation. However, the pyritization of biogenic magnetite likely proceeds via a complex interplay of these factors, with organic matter playing a key role in controlling pyrite morphology.

Spheroids vs. framboids—similarities and differences

Framboidal pyrite is commonly used to track microbial sulfur cycling in modern and ancient environments. This, however, requires that the analyzed precipitates are pristine products of primary geomicrobiological processes. While lacking the diagnostic raspberry-like internal texture, pyrite spheroids in our experiment approximate pyrite framboids in anoxic and sulfidic sediments concerning the overall spherical habit, aggregational texture, and size (~3–5 μm)[86]. Moreover, the organic matter-mediated formation of pyrite spheroids in our experiment is broadly analogous to mechanisms proposed for generating pyrite framboids in sedimentary deposits, including sulfate-reducing biofilms or microbial mats[54–56]. This suggests that in the presence of biogenic (i.e., organic matter-associated) precursor iron minerals and S^0, framboid-like pyrite spheroids could form in the same environments as true framboids. Moreover, petrographic observations suggest that diagenetic and hydrothermal alteration of pyrite framboids can induce infilling and recrystallization processes that drive their textural evolution towards spherical precipitates that do not exhibit pristine internal textures[87]. Indeed, some pyrite in ancient rocks described as framboids show an overall spherical habit but lack the internal texture of pristine framboids (e.g.,[10,57,88]). While our findings do not refute that these precipitates are indeed infilled or recrystallized framboids[10,89], we suggest that some of such pyrite may have been originally pyrite spheroids, particularly in hydrothermal environments.

Spheroids as biosignatures for iron-cycling microorganisms?

We demonstrated that the hydrothermal sulfidation of biogenic magnetite can drive the formation of framboid-like pyrite. Consistent with previous experimental studies[59], this indicates that microbial sulfur cycling is not necessarily the critical mechanism for forming framboid-like pyrite, meaning that such precipitates may not be specific biosignatures for sulfur-cycling microorganisms. Instead, framboid-like pyrite may be the product of the diagenetic transformation of biogenic iron minerals, such as magnetite produced by dissimilatory Fe(III)-reducing prokaryotes or magnetotactic bacteria, under sulfidic conditions (Fig. 7c). Framboid-like pyrite may result from the sulfidation of biogenic magnetite irrespective of whether reduced sulfur species are biogenic (i.e., from microbial sulfur cycling) or abiogenic (e.g., volcanogenic) in origin. This means framboid-like pyrite may be a promising taphonomic fingerprint of precursor biominerals resulting from microbial iron cycling, particularly in hydrothermal sulfide systems.

Conclusions

We demonstrated that sulfidation of abiogenic and biogenic magnetite yields pyrite under sulfidic hydrothermal conditions. Pyritization rates and pyrite morphology were strongly controlled by S^0 (S^0 promoting pyritization; cubic-euhedral without S^0, octahedral-dendritic with S^0), pH (octahedral-dendritic at pH 7, cubic euhedral at pH 7.5), and organic matter (inhibiting pyritization). Notably, S^0 and organic matter promoted the formation of ~3–5 μm pyrite spheroids that resembled pyrite framboids, demonstrating that framboid-like pyrite can form via the hydrothermal sulfidation of biogenic magnetite under sulfidic conditions. This suggests that some framboid-like pyrite in ancient rocks may represent original pyrite spheroids rather than recrystallized or infilled pyrite framboids, particularly in hydrothermal deposits. Moreover, our study highlights the need to constrain the impact of diagenetic processes on pyrite morphologies. Framboid-like pyrite may represent a taphonomic product from the sulfidation of biogenic magnetite. Therefore, framboid-like pyrite is not only a potential fingerprint of microbial sulfur cycling but can also record microbial iron cycling in hydrothermal systems.

Methods

Starting materials

For experiments with abiogenic magnetite (i.e., without organic matter), we synthesized magnetite nanoparticles in an N_2-filled anoxic chamber according to previously described procedures[34]. For experiments with biogenic magnetite (i.e., with organic matter), we prepared magnetite nanoparticles via dissimilatory Fe(III)-reduction of 2-line ferrihydrite by *Geobacter sulfurreducens*. The 2-line ferrihydrite was prepared by reaction of $Fe(NO_3)_3{\cdot}9H_2O$ (40 g) with KOH (1 M) until pH 7.0[90]. The material was centrifuged (26000 × *g*; 10 min) and washed three times in Milli-Q H_2O to remove nitrate ions and then purged with N_2 to remove O_2. A dense culture of *G. sulfurreducens* was inoculated at 10% (v/v) in a total volume of 100 mL growth medium in a 200 mL serum bottle and closed with butyl stoppers. The growth medium contained 30 mM $NaHCO_3$, 25 mM Na acetate, 40 mM Na fumarate, and 1 mL each of SL-10 trace element solution, seven vitamin solution, and selenite-tungstate solution[91]. In the late exponential phase (after ~48 h, OD_{600}~0.5), the cells were centrifuged at (5300 × *g*; 20 min) and washed in 50 mL of 10 mM HEPES buffer solution (pH 7.0) three times. The resulting cell pellets were resuspended in 10 mM HEPES buffer solution and then added at $OD_{600} = 0.38$ to a Fe(III)-reduction medium containing 10 mM HEPES buffer, 25 mM Na acetate, and 50 mM 2-line ferrihydrite at 30 °C for three days. The dissimilatory Fe(III)-reduction was conducted in 25 mL total volume in 50 mL serum bottles closed with butyl stoppers. Anoxic and sterile conditions were maintained during all steps in the preparation of biogenic magnetite.

Both abiogenic and biogenic magnetite were washed by holding the particles in place, placing a hand-magnet to the outside of the serum bottle, decanting the supernatant, adding ~80 mL O_2-free ultrapure H_2O (Milli-Q, Merck Millipore), and sonicating for 5 min. This procedure was repeated two times. The total organic carbon contents (TOC) of the abiogenic and biogenic magnetite suspensions were determined as the sum of the dissolved organic carbon (DOC) in the liquid phase and the organic carbon content of the solid phase (Supplementary Table 1). After centrifugation at 12,100 × *g* for 5 min, the DOC of the liquid phase was analyzed using a Multi N/C analyzer 2100S (Analytik Jena GmbH) as the non-purgeable organic carbon after acidification with 50 μL of 2 M HCl. For organic carbon analyses of the solid phase, samples were dried at 50 °C and powdered with a ball mill. Double determination analysis was conducted using a Vario Cube Elemental Analyzer (Elementar Analysesysteme GmbH), and quantification was done using the sulfanilamide standard. The resulting TOC of the

abiogenic and biogenic magnetite suspensions were 0.98 mM and 9.29 mM, respectively. The average crystallite sizes of the synthesized abiogenic and biogenic magnetite (confirmed by μ-XRD; Supplementary Fig. 2), as calculated using the Scherrer equation[92], were 12 nm and 9 nm, respectively.

Artificial seawater was prepared using 17.30 g/L NaCl, 8.61 g/L $MgCl_2$•$6H_2O$, 0.03 g/L $MgSO_4$•$7H_2O$, 0.99 g/L $CaCl_2$•$2H_2O$, 0.39 g/L KCl, 0.06 g/L KBr, 0.25 g/L NH_4Cl, and 1.85 g/L $NaHCO_3$. The pH of the resulting solution was adjusted to 7.0 using 1 M HCl, and dissolved O_2 was degassed by purging with 50/50 N_2/CO_2. An anoxic 1 M sulfide solution was made by dissolving Na_2S in O_2-free ultrapure H_2O. Colloidal S^0 was prepared by dropwise addition of 10 mL concentrated H_2SO_4 to 30 mL 3 M Na-thiosulfate [$Na_2S_2O_3 \times 5H_2O$] solution, which was immersed in an ice bath. Precipitation of colloidal S^0 in this process yielded a yellow suspension. The aggregation of colloidal S^0 was induced by the addition of 40 mL saturated NaCl solution. To remove excess NaCl, the colloidal S^0 was allowed to settle overnight, the supernatant was removed, and 50 mL of 2% NaCl was added. This process was repeated three times. The resulting suspension was transferred to a serum bottle and purged with N_2 to remove O_2. The concentration of the colloidal S^0 stock was determined gravimetrically after drying an aliquot at 60 °C.

Experimental setups

The preparation of incubation experiments, sampling, and sample preparation for analysis were conducted in an N_2-filled anoxic chamber. Batch experiments were prepared with total volumes of 50 mL in 100 mL-volume serum bottles closed with butyl stoppers to prevent the presence of oxygen. We used a minimum of two experimental replicates for chemical analysis (pH, sequential iron extraction). At least one additional replicate per setup was prepared for mineralogical analysis (Raman spectroscopy, μ-XRD) and SEM.

The magnetite suspensions and the sulfide solution were added to the artificial seawater at 60 mM sulfide and 15 mM iron (4:1 molar ratio). This mixing ratio resulted in 0.14 mM and 1.3 mM added TOC from abiogenic and biogenic magnetite, respectively. To each experimental setup, 100 mM MOPS buffer was added, which resulted in an average initial pH of 7.46 ± 0.06 (Supplementary Fig. 3). During the experiment, the pH remained constant within ±0.1 pH units (i.e., decreased to 7.38 ± 0.03; Supplementary Fig. 3). For both abiogenic and biogenic magnetite experiments, we prepared two additional setups that further contained 62 mM of commercially available crystalline S^0 (100 mg, Sigma–Aldrich, product # 13803) or pre-synthesized colloidal S^0 (suspended in 2% NaCl solution), respectively. Light microscopy observations indicate that crystalline S^0 particles were ~30 μm while colloidal S^0 particles were ≤5 μm in size. All serum bottles were incubated at 80 °C.

Geochemical analyses

Aliquots (0.5 mL) of the mineral suspension were centrifuged for 5 min at 12,100 × *g* to separate the minerals from the aqueous phase (this phase contains both the combined dissolved and colloidal iron that did not settle during centrifugation). Concentrations of Fe^{2+} in the aqueous phase and total iron in the solid phase were quantified spectrophotometrically using the ferrozine assay[93]. Supernatants were acidified with 1 M HCl before analysis. Sequential iron extraction of the solid phase using 6 M HCl (reactive iron minerals: magnetite, mackinawite, and greigite) and 8 M HNO_3 (pyrite) was used to determine the degree of pyritization over time[94,95]. Extraction with 6 M HCl was conducted for 24 h in an anoxic chamber in the presence of Ti(III)-citrate to prevent oxidation of dissolved sulfide to S^0, which could reduce iron extraction yields[96]. Solid residues from the 6 M HCl extraction step were extracted with 8 M HNO_3 for >2 h. Centrifuged aliquots of the liquid phase were analyzed in duplicates for the presence of polysulfides via UV-Vis spectroscopy in 96-well plates using a spectral range of 250–500 nm. The resulting spectra were normalized using a Milli-Q blank.

μ-X-ray diffraction (μ-XRD)

Aliquots for μ-XRD measurements were taken in an N_2-filled anoxic chamber. Mineral pellets were harvested by centrifugation and washed three times with anoxic ultrapure water to remove residual salts before drying. Dry samples were stored in N_2-filled preserving jars until μ-XRD analysis under ambient atmospheric conditions[97,98]. μ-XRD was performed on dry material using a Bruker's D8 Discover GADDS XRD^2 micro-diffractometer equipped with a standard sealed tube with a copper-anode (Co Kα radiation, λ = 0.179 nm) at 30 kV/30 mA. The total time measurement was 240 s at two detector positions (15° and 40°). Phase identification was validated using the Match! Software for phase identification from powder diffraction (Match!, Crystal Impact, Bonn, Germany, version 3.11.5.203) with the Crystallography Open Database (COD-Inorg REV211633 2018.19.25).

Raman spectroscopy

Aliquots from suspended samples were dried onto glass slides in an anoxic chamber. Glass slides were transported to the instrument in N_2-filled jars. Raman spectra were acquired with an Alpha 500R Confocal Raman Microscope (WITec GmbH, Ulm, Germany), which was equipped with a 532 nm excitation laser, a UHTS 300 spectrometer, and a DV401-BV CCD camera. The optical grating was 600 g/mm for recording the spectra from 0 to 3790 cm^{-1}. A 40× objective with a numerical aperture of 0.6 was used (EC Epiplan-neofluor, Carl Zeiss, Germany). The laser power was adjusted to ≤1 mW using an optical power meter (PM100D, Thorlabs GmbH, Dachau, Germany) to avoid heat-induced mineral transformation. Three spots were analyzed per sample using up to 10 integrations of 10–20 s each. Spectra from these three spot measurements were combined into a composite spectrum, and relative intensities were normalized to 100. Pyrite was identified using the software CrystalSleuth, the RRUFF database (https://rruff.info/; accessed 16 August 2023), and Fe(III)- FeS_m was compared to reference patterns from Bourdoiseau et al.[63].

Scanning electron microscopy (SEM) and focused-ion-beam (FIB) milling

Aliquots from experimental duplicates were pooled and washed three times with anoxic Milli-Q water. These samples were dried onto a carbon adhesive tab attached to an aluminum stub in an anoxic chamber. Once dry, the samples were coated with 8 nm of gold using a BAL-TEC SCD 005 sputter coater to reduce charging effects during analysis. Morphological characterization of experimental products was performed using a Crossbeam 550L SEM (Zeiss, Oberkochen, Germany) operating at an acceleration voltage of 2 kV and working distances of 5.2 mm. All micrographs were taken using the Secondary Electron Secondary Ion (SESI) detector.

FIB milling was performed on a Zeiss Crossbeam 550L. A SEM stub was coated with a thin layer of Tempfix (Plano G3305). The coated stub was held at a temperature of approximately 40 °C and the anoxically dried sample was sprinkled onto its surface. After reaching room temperature, the sample was sputter-coated with 8 nm of platinum. A cross-section through the object of interest was made using the 300 pA–30 kV FIB probe. In a second step, the surface of the cross-section was polished using the 2 pA–30 kV FIB probe. Images were generated using the InLens detector at an acceleration voltage of 5 kV and a probe current of 100 pA.

Reporting summary

Further information on research design is available in the Nature Portfolio Reporting Summary linked to this article.

Data availability

The data supporting this study's findings are available within the paper and its Supplementary Materials and through an online repository using the following link: https://doi.org/10.6084/m9.figshare.25539925. Any additional information is available from the corresponding authors upon reasonable request.

Received: 24 October 2023; Accepted: 17 April 2024;
Published online: 15 May 2024

References

1. McCollom, T. M. & Seewald, J. S. Abiotic synthesis of organic compounds in deep-sea hydrothermal environments. *Chem. Rev.* **107**, 382–401 (2007).
2. Russell, M. J., Hall, A. J. & Martin, W. Serpentinization as a source of energy at the origin of life: serpentinization and the emergence of life. *Geobiology* **8**, 355–371 (2010).
3. Mißbach, H. et al. Assessing the diversity of lipids formed via Fischer-Tropsch-type reactions. *Org. Geochem.* **119**, 110–121 (2018).
4. Baross, J. A. & Hoffman, S. E. Submarine hydrothermal vents and associated gradient environments as sites for the origin and evolution of life. *Orig. Life Evol. Biosph.* **15**, 327–345 (1985).
5. Martin, W., Baross, J., Kelley, D. & Russell, M. J. Hydrothermal vents and the origin of life. *Nat. Rev. Microbiol.* **6**, 805–814 (2008).
6. Rasmussen, B. Filamentous microfossils in a 3,235-million-year-old volcanogenic massive sulphide deposit. *Nature* **405**, 676–679 (2000).
7. Van Kranendonk, M., Philippot, P., Lepot, K., Bodorkos, S. & Pirajno, F. Geological setting of Earth's oldest fossils in the ca. 3.5 Ga Dresser Formation, Pilbara Craton, Western Australia. *Precambrian Res.* **167**, 93–124 (2008).
8. Dodd, M. S. et al. Evidence for early life in Earth's oldest hydrothermal vent precipitates. *Nature* **543**, 60–64 (2017).
9. Duda, J.-P. et al. Ideas and perspectives: hydrothermally driven redistribution and sequestration of early Archaean biomass—the "hydrothermal pump hypothesis". *Biogeosciences* **15**, 1535–1548 (2018).
10. Runge, E. A., Mansor, M., Kappler, A. & Duda, J.-P. Microbial biosignatures in ancient hydrothermal sulfides. *Geobiology* **21(3)**, 355-377 (2023).
11. Franz, H. B. et al. Large sulfur isotope fractionations in Martian sediments at Gale crater. *Nat. Geosci.* **10**, 658–662 (2017).
12. Hsu, H.-W. et al. Ongoing hydrothermal activities within Enceladus. *Nature* **519**, 207–210 (2015).
13. Li, Y.-L., Konhauser, K. O. & Zhai, M. The formation of magnetite in the early Archean oceans. *Earth Planet. Sci. Lett.* **466**, 103–114 (2017).
14. Ozturk, S. F. & Sasselov, D. D. On the origins of life's homochirality: inducing enantiomeric excess with spin-polarized electrons. *Proc. Natl. Acad. Sci. USA* **119**, e2204765119 (2022).
15. Kirschvink, J. L. & Chang, S.-B. R. Ultrafine-grained magnetite in deep-sea sediments: possible bacterial magnetofossils. *Geology* **12**, 559–562 (1984).
16. Hansel, C. M., Benner, S. G. & Fendorf, S. Competing Fe(II)-induced mineralization pathways of ferrihydrite. *Environ. Sci. Technol.* **39**, 7147–7153 (2005).
17. Amor, M., Tharaud, M., Gélabert, A. & Komeili, A. Single-cell determination of iron content in magnetotactic bacteria: implications for the iron biogeochemical cycle. *Environ. Microbiol.* **22**, 823–831 (2020).
18. Vargas, M., Kashefi, K., Blunt-Harris, E. L. & Lovley, D. R. Microbiological evidence for Fe(III) reduction on early Earth. *Nature* **395**, 65–67 (1998).
19. Lin, W. et al. Origin of microbial biomineralization and magnetotaxis during the Archean. *Proc. Natl Acad. Sci. USA* **114**, 2171–2176 (2017).
20. Suzuki, Y., Inagaki, F., Takai, K., Nealson, K. H. & Horikoshi, K. Microbial diversity in inactive chimney structures from deep-sea hydrothermal systems. *Microb. Ecol.* **47**, 186–196 (2004).
21. Roh, Y. et al. Metal reduction and iron biomineralization by a psychrotolerant Fe(III)-reducing bacterium, *Shewanella* sp. strain PV-4. *Appl. Environ. Microbiol.* **72**, 3236–3244 (2006).
22. Lin, J. T. et al. Magnetite formation from ferrihydrite by hyperthermophilic archaea from Endeavour Segment, Juan de Fuca Ridge hydrothermal vent chimneys. *Geobiology* **12**, 200–211 (2014).
23. Nakano, S. et al. Bullet-shaped magnetosomes and metagenomic-based magnetosome gene profiles in a deep-sea hydrothermal vent chimney. *Front. Microbiol.* **14**, 1174899 (2023).
24. Kashefi, K. & Lovley, D. R. Extending the upper temperature limit for life. *Science* **301**, 934 (2003).
25. Thomas-Keprta, K. L. et al. Elongated prismatic magnetite crystals in ALH84001 carbonate globules: potential Martian magnetofossils. *Geochim. Cosmochim. Acta* **64**, 4049–4081 (2000).
26. Carvallo, C. et al. Biogenic vs. abiogenic magnetite nanoparticles: a XMCD study. *Am. Mineral.* **93**, 880–885 (2008).
27. Lam, K. P. et al. Characterizing magnetism of individual magnetosomes by X-ray magnetic circular dichroism in a scanning transmission X-ray microscope. *Chem. Geol.* **270**, 110–116 (2010).
28. Amor, M. et al. Chemical signature of magnetotactic bacteria. *Proc. Natl Acad. Sci. USA* **112**, 1699–1703 (2015).
29. Amor, M. et al. Key signatures of magnetofossils elucidated by mutant magnetotactic bacteria and micromagnetic calculations. *JGR Solid Earth* **127**, e2021JB023239 (2022).
30. Han, X. et al. Using Zn and Ni behavior during magnetite precipitation in banded iron formations to determine its biological or abiotic origin. *Earth Planet. Sci. Lett.* **568**, 117052 (2021).
31. Kappler, A., Thompson, A. & Mansor, M. Impact of biogenic magnetite formation and transformation on biogeochemical cycles. *Elements* **19**, 222–227 (2023).
32. Früh-Green, G. L. et al. Diversity of magmatism, hydrothermal processes and microbial interactions at mid-ocean ridges. *Nat. Rev. Earth Environ.* **3**, 852–871 (2022).
33. Reysenbach, A.-L. & Cady, S. L. Microbiology of ancient and modern hydrothermal systems. *Trends Microbiol.* **9**, 79–86 (2001).
34. Runge, E. A. et al. Sulfidation of nano-magnetite to pyrite: implications for interpreting paleoenvironmental proxies and biosignature records in hydrothermal sulfide deposits. *Earth Planet. Sci. Lett.* **617**, 118261 (2023).
35. Canfield, D. E. & Berner, R. A. Dissolution and pyritization of magnetite in anoxic marine sediments. *Deep Sea Res. Part B Oceanogr. Lit. Rev.* **51**, 645–659 (1987).
36. Poulton, S. W., Krom, M. D. & Raiswell, R. A revised scheme for the reactivity of iron (oxyhydr)oxide minerals towards dissolved sulfide. *Geochim. Cosmochim. Acta* **68**, 3703–3715 (2004).
37. Qian, G., Brugger, J., Skinner, W. M., Chen, G. & Pring, A. An experimental study of the mechanism of the replacement of magnetite by pyrite up to 300 °C. *Geochim. Cosmochim. Acta* **74**, 5610–5630 (2010).
38. Qian, G., Brugger, J., Testemale, D., Skinner, W. & Pring, A. Formation of As(II)-pyrite during experimental replacement of magnetite under hydrothermal conditions. *Geochim. Cosmochim. Acta* **100**, 1–10 (2013).
39. Bendt, G., Saddeler, S. & Schulz, S. Sulfidation of magnetite nanoparticles—following the polysulfide pathway. *Eur. J. Inorg. Chem.* **602**, 608 (2019).
40. Nie, M. et al. Effect of stoichiometry on nanomagnetite sulfidation. *Environ. Sci. Technol*. https://doi.org/10.1021/acs.est.2c08179 (2023).
41. Benning, L. G., Wilkin, R. T. & Barnes, H. L. Reaction pathways in the Fe–S system below 100 °C. *Chem. Geol.* **167**, 25–51 (2000).
42. Gong, M., Kirkeminde, A. & Ren, S. Symmetry-defying iron pyrite (FeS2) nanocrystals through oriented attachment. *Sci. Rep.* **3**, 2092 (2013).
43. Peiffer, S. et al. Pyrite formation and mineral transformation pathways upon sulfidation of ferric hydroxides depend on mineral type and sulfide concentration. *Chem. Geol.* **400**, 44–55 (2015).
44. Wan, M., Schröder, C. & Peiffer, S. Fe(III):S(-II) concentration ratio controls the pathway and the kinetics of pyrite formation during sulfidation of ferric hydroxides. *Geochim. Cosmochim. Acta* **217**, 334–348 (2017).

45. Hockmann, K., Planer-Friedrich, B., Johnston, S. G., Peiffer, S. & Burton, E. D. Antimony mobility in sulfidic systems: coupling with sulfide-induced iron oxide transformations. *Geochim. Cosmochim. Acta* **282**, 276–296 (2020).
46. Baya, C. et al. Influence of trace level As or Ni on pyrite formation kinetics at low temperature. *Geochim. Cosmochim. Acta* **300**, 333–353 (2021).
47. Wang, Q. et al. Transformations of ferrihydrite–extracellular polymeric substance coprecipitates driven by dissolved sulfide: interrelated effects of carbon and sulfur loadings. *Environ. Sci. Technol*. https://doi.org/10.1021/acs.est.2c06921 (2023).
48. Domingos, J. M. et al. Inferred pyrite growth via the particle attachment pathway in the presence of trace metals. *Geochem. Persp. Lett.* **26**, 14–19 (2023).
49. Wilkin, R. T. & Barnes, H. L. Pyrite formation by reactions of iron monosulfides with dissolved inorganic and organic sulfur species. *Geochim. Cosmochim. Acta* **60**, 4167–4179 (1996).
50. Morse, J. W. & Wang, Q. Pyrite formation under conditions approximating those in anoxic sediments: II. Influence of precursor iron minerals and organic matter. *Mar. Chem.* **57**, 187–193 (1997).
51. Rickard, D., Butler, I. B. & Oldroyd, A. A novel iron sulphide mineral switch and its implications for Earth and planetary science. *Earth Planet. Sci. Lett.* **189**, 85–91 (2001).
52. ThomasArrigo, L. K., Bouchet, S., Kaegi, R. & Kretzschmar, R. Organic matter influences transformation products of ferrihydrite exposed to sulfide. *Environ. Sci. Nano* **7**, 3405–3418 (2020).
53. Hiemstra, T., Mendez, J. C. & Li, J. Evolution of the reactive surface area of ferrihydrite: time, pH, and temperature dependency of growth by Ostwald ripening. *Environ. Sci. Nano* **6**, 820–833 (2019).
54. Popa, R., Kinkle, B. K. & Badescu, A. Pyrite framboids as biomarkers for iron-sulfur systems. *Geomicrobiol. J.* **21**, 193–206 (2004).
55. Maclean, L. C. W. et al. A high-resolution chemical and structural study of framboidal pyrite formed within a low-temperature bacterial biofilm. *Geobiology* **6**, 471–480 (2008).
56. Wacey, D. et al. Uncovering framboidal pyrite biogenicity using nano-scale CNorg mapping. *Geology* **43**, 27–30 (2015).
57. Duda, J.-P. et al. A rare glimpse of paleoarchean life: geobiology of an exceptionally preserved microbial mat facies from the 3.4 Ga Strelley Pool Formation, Western Australia. *PLoS ONE* **11**, e0147629 (2016).
58. Duverger, A. et al. Mechanisms of pyrite formation promoted by sulfate-reducing bacteria in pure culture. *Front. Earth Sci.* **8**, 588310 (2020).
59. Duverger, A., Bernard, S., Viennet, J., Miot, J. & Busigny, V. Formation of pyrite spherules from mixtures of biogenic FeS and organic compounds during experimental diagenesis. *Geochem. Geophys. Geosyst.* https://doi.org/10.1029/2021GC010056 (2021).
60. Berg, J. S. et al. Rapid pyritization in the presence of a sulfur/sulfate-reducing bacterial consortium. *Sci. Rep.* **10**, 8264 (2020).
61. Truong, C. et al. Production of carbon-containing pyrite spherules induced by hyperthermophilic Thermococcales: a biosignature? *Front. Microbiol.* **14**, 1145781 (2023).
62. Ohfuji, H. & Rickard, D. Experimental syntheses of framboids—a review. *Earth Sci. Rev.* **71**, 147–170 (2005).
63. Bourdoiseau, J.-A., Jeannin, M., Sabot, R., Rémazeilles, C. & Refait, P. H. Characterisation of mackinawite by Raman spectroscopy: effects of crystallisation, drying and oxidation. *Corros. Sci.* **50**, 3247–3255 (2008).
64. Steudel, R. & Chivers, T. The role of polysulfide dianions and radical anions in the chemical, physical and biological sciences, including sulfur-based batteries. *Chem. Soc. Rev.* **48**, 3279–3319 (2019).
65. Vorlicek, T. P., Kahn, M. D., Kasuya, Y. & Helz, G. R. Capture of molybdenum in pyrite-forming sediments: role of ligand-induced reduction by polysulfides. *Geochim. Cosmochim. Acta* **68**, 547–556 (2004).
66. Csákberényi-Malasics, D. et al. Structural properties and transformations of precipitated FeS. *Chem. Geol.* **294–295**, 249–258 (2012).
67. Picard, A., Gartman, A., Clarke, D. R. & Girguis, P. R. Sulfate-reducing bacteria influence the nucleation and growth of mackinawite and greigite. *Geochim. Cosmochim. Acta* **220**, 367–384 (2018).
68. Noël, V. et al. FeS colloids—formation and mobilization pathways in natural waters. *Environ. Sci. Nano* **7**, 2102–2116 (2020).
69. Hartler, N., Libert, J. & Teder, A. Rate of sulfur dissolution in aqueous sodium sulfide. *Ind. Eng. Chem. Proc. Des. Dev.* **6**, 398–406 (1967).
70. Avetisyan, K., Buchshtav, T. & Kamyshny, A. Kinetics and mechanism of polysulfides formation by a reaction between hydrogen sulfide and orthorhombic cyclooctasulfur. *Geochim. Cosmochim. Acta* **247**, 96–105 (2019).
71. Chadwell, S. J., Rickard, D. & Luther, G. W. Electrochemical evidence for metal polysulfide complexes: tetrasulfide (S2-4) reactions with Mn2+, Fe2+, Co2+, Ni2+, Cu2+, and Zn2+. *Electroanalysis* **13**, 21–29 (2001).
72. Illés, E. & Tombácz, E. The effect of humic acid adsorption on pH-dependent surface charging and aggregation of magnetite nanoparticles. *J. Colloid Interface Sci.* **295**, 115–123 (2006).
73. Matamoros-Veloza, A., Stawski, T. M. & Benning, L. G. Nanoparticle assembly leads to mackinawite formation. *Cryst. Growth Des.* **18**, 6757–6764 (2018).
74. Ma, H. et al. Secondary mineral formation and carbon dynamics during FeS oxidation in the presence of dissolved organic matter. *Environ. Sci. Technol.* **56**, 14120–14132 (2022).
75. Rickard, D. T. Kinetics and mechanism of pyrite formation at low temperatures. *Am. J. Sci.* **275**, 636–652 (1975).
76. Yao, W. & Millero, F. J. Oxidation of hydrogen sulfide by hydrous Fe(III) oxides in seawater. *Mar. Chem.* **52**, 1–16 (1996).
77. Yu, Z.-G., Peiffer, S., Göttlicher, J. & Knorr, K.-H. Electron transfer budgets and kinetics of abiotic oxidation and incorporation of aqueous sulfide by dissolved organic matter. *Environ. Sci. Technol.* **49**, 5441–5449 (2015).
78. Cosmidis, J., Nims, C. W., Diercks, D. & Templeton, A. S. Formation and stabilization of elemental sulfur through organomineralization. *Geochim. Cosmochim. Acta* **247**, 59–82 (2019).
79. Picard, A. et al. Authigenic metastable iron sulfide minerals preserve microbial organic carbon in anoxic environments. *Chem. Geol.* **530**, 119343 (2019).
80. Raven, M. R., Sessions, A. L., Adkins, J. F. & Thunell, R. C. Rapid organic matter sulfurization in sinking particles from the Cariaco Basin water column. *Geochim. Cosmochim. Acta* **190**, 175–190 (2016).
81. Son, S., Pil Hyun, S., Charlet, L. & Kwon, K. D. Thermodynamic stability reversal of iron sulfides at the nanoscale: insights into the iron sulfide formation in low-temperature aqueous solution. *Geochim. Cosmochim. Acta* **338**, 220–228 (2022).
82. Murowchick, J. B. & Barnes, H. L. Effects of temperature and degree of supersaturation on pyrite morphology. *Am. Mineral.* **72**, 1241–1250 (1987).
83. Wang, S. et al. Constraints on fluid evolution and growth processes of black smoker chimneys by pyrite geochemistry: a case study of the Tongguan hydrothermal field, South Mid-Atlantic Ridge. *Ore Geol. Rev.* **140**, 104410 (2022).
84. Butler, I. B. & Rickard, D. Framboidal pyrite formation via the oxidation of iron (II) monosulfide by hydrogen sulphide. *Geochim. Cosmochim. Acta* **64**, 2665–2672 (2000).
85. ThomasArrigo, L. K., Byrne, J. M., Kappler, A. & Kretzschmar, R. Impact of organic matter on iron(II)-catalyzed mineral transformations in ferrihydrite–organic matter coprecipitates. *Environ. Sci. Technol.* **52**, 12316–12326 (2018).
86. Rickard, D. Sedimentary pyrite framboid size-frequency distributions: a meta-analysis. *Palaeogeogr. Palaeoclimatol. Palaeoecol.* **522**, 62–75 (2019).

87. Liu, K. et al. Morphology of framboidal pyrite and its textural evolution: evidence from the Logatchev area, Mid-Atlantic Ridge. *Ore Geol. Rev.* **141**, 104630 (2022).
88. Reitner, J., Blumenberg, M., Walliser, E.-O., Schäfer, N. & Duda, J.-P. Methane-derived carbonate conduits from the late Aptian of Salinac (Marne Bleues, Vocontian Basin, France): petrology and biosignatures. *Mar. Pet. Geol.* **66**, 641–652 (2015).
89. Wilkin, R. T., Barnes, H. L. & Brantley, S. L. The size distribution of framboidal pyrite in modern sediments: an indicator of redox conditions. *Geochim. Cosmochim. Acta* **60**, 3897–3912 (1996).
90. Schwertmann, U. & Cornell, R. M. *Iron Oxides in the Laboratory* (Wiley, 2000).
91. Tomaszewski, E. J. et al. Complexation by cysteine and iron mineral adsorption limit cadmium mobility during metabolic activity of *Geobacter sulfurreducens*. *Environ. Sci. Processes Impacts* **22**, 1877–1887 (2020).
92. Mansor, M., Berti, D., Hochella, M. F., Murayama, M. & Xu, J. Phase, morphology, elemental composition, and formation mechanisms of biogenic and abiogenic Fe-Cu-sulfide nanoparticles: a comparative study on their occurrences under anoxic conditions. *Am. Mineral.* **104**, 703–717 (2019).
93. Stookey, L. L. Ferrozine—a new spectrophotometric feagent for iron. *Anal. Chem.* **42**, 779–781 (1970).
94. Heron, G., Crouzet, C., Bourg, A. C. & Christensen, T. H. Speciation of Fe(II) and Fe(III) in contaminated aquifer sediments using chemical extraction techniques. *Environ. Sci. Technol.* **28**, 1698–1705 (1994).
95. Huerta-Diaz, M. A. & Morse, J. W. A quantitative method for determination of trace metal concentrations in sedimentary pyrite. *Mar. Chem.* **29**, 119–144 (1990).
96. Rickard, D. et al. The composition of nanoparticulate mackinawite, tetragonal iron(II) monosulfide. *Chem. Geol.* **235**, 286–298 (2006).
97. Boursiquot, S., Mullet, M., Abdelmoula, M., Génin, J.-M. & Ehrhardt, J.-J. The dry oxidation of tetragonal FeS 1- x mackinawite. *Phys. Chem. Miner.* **28**, 600–611 (2001).
98. Zhang, Q. et al. Humidity related magnetite alteration in an experimental setup. *Geophys. J. Int.* **224**, 69–85 (2020).

Acknowledgements

We thank François Guyot and two anonymous reviewers for their constructive feedback. This study was supported by the DFG (SPP 1833, Emmy Noether Programme; DU 1450/3-2, DU 1450/7-1; J.P.D., E.R.; INST 37/1027-1 FUGG; A.K.) as well as by the German Excellence Strategy of the German Federal and State Governments (EXC2124, 390838134; Tübingen Structural Microscopy Core Facility; A.K., M.M., S.F., J.S.). We thank James M. Byrne for advice on preparing biogenic magnetite and Prachi Joshi, Aude Picard, and Julie Cosmidis for helpful discussions on the experimental design. Jorinel-Manuel Domingos kindly provided colloidal S^0. Eva Voggenreiter and Johann Holdt helped with TOC analysis. Dominique J. Lunter and Hans Schönfelder are thanked for their assistance with Raman spectroscopy.

Author contributions

E.R., M.M., A.K. and J.-P.D. planned and designed the experiment. E.R. and T.H.C. prepared abiogenic and biogenic magnetite. E.R. conducted the experiments and analyzed the data. J.S. and S.F. performed FIB and SEM analysis. T.H.C. performed µ-XRD analysis and prepared FIB and TOC samples. All authors contributed to the discussion of results and writing.

Funding

Open Access funding enabled and organized by Projekt DEAL.

Competing interests

The authors declare no competing interests.

Additional information

Supplementary information The online version contains supplementary material available at https://doi.org/10.1038/s43247-024-01400-z.

Correspondence and requests for materials should be addressed to Eric Runge or Jan-Peter Duda.

Peer review information *Communications Earth & Environment* thanks Hiroaki Ohfuji, Francois Guyot, and the other, anonymous, reviewer(s) for their contribution to the peer review of this work. Primary Handling Editors: Carolina Ortiz Guerrero. A peer review file is available.